Rare Metal Materials and Engineering
Volume 49, Issue 3, March 2020
Available online at www.rmme.ac.cn

Science Press

Cite this article as: Rare Metal Materials and Engineering, 2020, 49(3): 0787-0796.

ARTICLE

A Newly Designed Radiation Shielding Composite by MCNP and Fabricated by SPS Followed by Hot-rolling

Zhang Yuyang[1], Wang Wenxian[1], Chen Hongsheng[1,2], Liu Ruifeng[1], Zhang Yuanqi[1], Shi Ning[1]

[1] Shanxi Key Laboratory of Advanced Magnesium-based Materials, Taiyuan University of Technology, Taiyuan 030024, China; [2] College of Mechanical and Vehicle Engineering, Taiyuan University of Technology, Taiyuan 030024, China

Abstract: A new kind of radiation shielding composite against both neutron and gamma rays was designed and fabricated. Based on Monte Carlo simulations, novel (W+B)/6061Al composite sheets with different W contents (40 wt%~70 wt%) were first fabricated by ball-milling and SPS (spark plasma sintering) followed by hot-rolling, and then the microstructure and mechanical properties were investigated. Results show that after rolling process, W and B particles are uniformly distributed in the matrix and the interface of W-Al exhibits a good metallurgical bonding in the form of solid solution. The composites mainly consist of W and Al phases. EBSD results show that W particles have the effects of promoting dynamic recrystallization (DRX) nucleation, confining the grain growth and reducing the texture of 6061Al matrix. Through tensile tests, the composite with 50 wt% W shows the highest strength and better plasticity. Together with the simulation results, composite with 50 wt% W is believed to meet the demand of practical applications. The strengthening mechanism of (W+B)/6061Al composites includes dislocation strengthening and load transfer effect.

Keywords: (W+B)/6061Al; radiation shielding composites; microstructure; mechanical properties; strengthening mechanisms

Nuclear energy, as the most potential future energy, is wildly utilized in the world. At the same time, with the rapid development of nuclear power industry, the resulting radiation hazards present great challenges to us[1]. Radiation shielding faces a variety of rays such as neutrons with different energies, gamma rays, secondary gamma rays and other charged particles. Among them, the shielding of neutrons and gamma rays should be a priority[2]. In previous studies, shielding concrete[3], boron steel[4], lead boron polyethylene[5], Al-B_4C composite[6] and cadmium[7] are generally used for shielding radiation. Although these materials can effectively attenuate the energy of neutrons or gamma rays, none of them (as monomer material) can satisfy the above-mentioned shielding properties at the same time. Besides, the strength and toughness are difficult to meet the requirements as structural shielding materials. Therefore, the newly developed material which can satisfy comprehensive shielding effect and achieve favorable physical and mechanical properties is one of the research hotspots nowadays[2].

Boron is extensively used in neutron shielding materials due to its favorable properties: the thermal neutron absorption cross section of ^{10}B is 3750 barn[8]. Compared with other neutron shielding elements (Hf, Sm, Eu, Gd, Dy and Cd), boron is more plentiful and less poisonous. Besides, the α-ray produced in the process of shielding is easier to be absorbed. Tungsten is very effective for shielding gamma and neutron radiation because of its high density, fast neutron removal cross section and fast neutron capture cross section[9]. Therefore, the combination of these two elements will achieve comprehensive shielding effect. In addition, using aluminum alloy as the matrix can achieve satisfactory mechanical properties and processability of the composites[10].

At present, the particle transport simulation program based on Monte Carlo method is used to calculate the

Received date: March 11, 2019
Foundation item: National Natural Science Foundation of China (51775366, 51805358)
Corresponding author: Wang Wenxian, Ph. D., Professor, College of Materials Science and Engineering, Taiyuan University of Technology, Taiyuan 030024, P. R. China, E-mail: wangwenxian@tyut.edu.cn

shielding performance of materials. The MCNP software developed by Los Alamos National Laboratory (USA) is mainly used to solve the problem of neutron, photon and electron transport and critical problem. Compared to other Monte Carlo softwares, MCNP has simpler and faster input program writing in solving the problem of shielding performance estimation of shielding materials.

Traditionally, the fabrication methods of aluminum matrix composites include stir-casting[11], hot isostatic pressing[12], squeeze casting[13], and powder metallurgy[14] etc. Spark plasma sintering (SPS) is an attractive sintering method for its fast heating and shorter holding time. The uniaxial pressure and pulsed DC current are applied to the powder simultaneously. The uniaxial pressure can help to achieve densification and break up the oxide layer of particles to facilitate neck formation[15]. The applied current can generate Joule heating at the particle contacts and high energy spark plasma at the gaps between particles[16]. Moreover, short processing time in SPS can avoid grain growth and realize effective bonding between particles[17].

In this study, using Monte-Carlo simulation, the relationship among the W/B content, plate thickness, radiation energy and neutron/gamma ray transmission ratio was obtained. The (W+B)/6061Al radiation shielding composites with different tungsten contents (40 wt%~70 wt%) were fabricated through ball-milling and SPS followed by hot-rolling. Then the influence of W content on microstructure and mechanical properties of the composites was studied. The relationship between the microstructure and mechanical properties was discussed and the mechanical mechanism was also analyzed.

1 Experiment

1.1 Material design

The physical model used in MCNP program is shown in Fig.1. The isotropic face source was used and the distance between the face source and incident plane in vacuum was 15 cm. The shielding material used in the model has the dimension of 10 cm×10 cm without defects, and the B, W particles are homogeneously distributed in the 6061Al alloy matrix. In order to obtain the shielding performance of the material against different radiations (neutron and gamma ray), different face sources were used separately. When simulating neutron radiation, the isotropic face source with energy of 0.0253 MeV was used. When simulating gamma ray radiation, the isotropic face sources with energy of 0~1 MeV and 1.25 MeV (^{60}Co) were used. The random sampling number was 8×10^7. The composition of materials used in the simulation was 30W-69Al-1B, 40W-59Al-1B, 50W-49Al-1B, 60W-39Al-1B and 70W-29Al-1B (wt%), which were designated as 30WAlB, 40WAlB, 50WAlB, 60WAlB and 70WAlB, respectively.

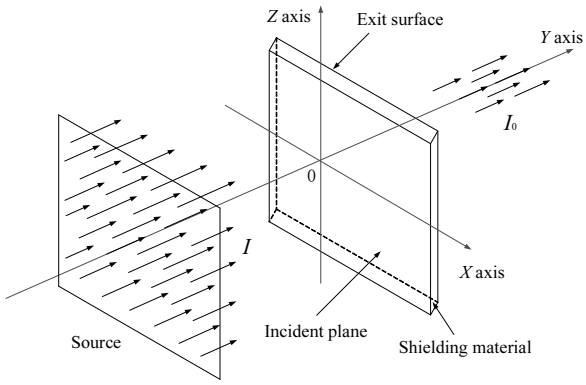

Fig.1 Sketch of physical model used in simulation

1.1.1 Simulation of neutron radiation

The neutron transmission ratio ($y=I_0/I$) of material can be calculated by the following equation[6]:

$$I_0 / I = \mathrm{e}^{-\Sigma x} \quad (1)$$

where I_0 and I stand for the neutron transmission intensity and incident intensity of the neutron, respectively. Σ is the macroscopic transmission cross section, x is the thickness of the shielding material.

Through simulation, the relationship between the neutron transmission ratio and thickness under different W contents is shown in Fig.2. From the simulation results, it can be seen that the neutron transmission ratio decreases with the increase of W particle content and the thickness of the material. When the thickness of all materials exceeds 3 cm, the neutron transmission ratio is less than 1%. Through the curve fitting, the relationship between the neutron transmission ratio and thickness of materials with different W contents was determined as follows: $y(30\ \text{wt\%})=\mathrm{e}^{-1.74174x}$, $y(40\ \text{wt\%})=\mathrm{e}^{-1.89881x}$, $y(50\ \text{wt\%})=\mathrm{e}^{-2.17795x}$, $y(60\ \text{wt\%})=\mathrm{e}^{-2.56168x}$, $y(70\ \text{wt\%})=\mathrm{e}^{-3.10464x}$.

1.1.2 Simulation of gamma ray radiation

When gamma rays pass through matter, they are absorbed by three kinds of interaction: photoelectric effect, Compton effect and electron pair effect, causing the attenuation of

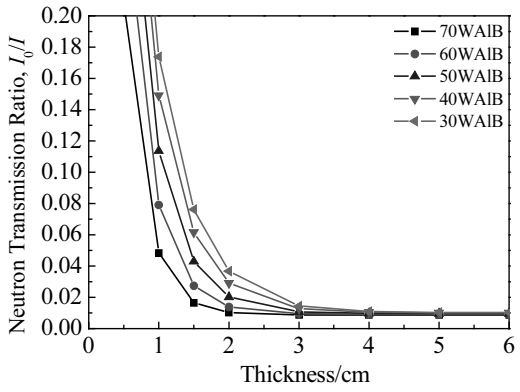

Fig.2 Relationship between the neutron transmission ratio and thickness of materials with different W contents

gamma rays. The extent of radiation attenuation depends on two aspects: the energy of the incident ray and the properties of absorbing matter. For rays with the same energy, the extent of attenuation depends mainly on the properties of the absorbing matter. Therefore, by measuring the attenuation coefficient of the absorbing material to the incident ray, we can quantitatively evaluate the radiation shielding performance of the measured material[18].

Linear attenuation coefficients are calculated from the exponential attenuation law:

$$N = N_0 e^{-\mu d} \quad (2)$$

where N_0 is initial intensity, N is transmission intensity, d is thickness of shielding material, and μ is total linear attenuation coefficient at a specific photon energy.

According to the simulation results of neutron radiation, the thickness of shielding material used was set as 3 cm. The relationship between the linear attenuation coefficient and energy at different W contents is shown in Fig.3. When the energy is less than 0.1 MeV, the linear attenuation coefficient of all materials goes to infinity. When the energy is in the range of 0.2~1 MeV, the linear attenuation coefficient decreases with the increase of energy. It is obvious that at the same energy, linear attenuation coefficient increases with the increase of W content, which means that improving the W content can significantly enhance the shielding performance of material.

In order to obtain the shielding performance of the material against specific gamma ray sources, ^{60}Co gamma ray with an average energy of 1.25 MeV was used as the isotropic face source. The linear attenuation coefficient μ (cm^{-1}) and the half value layer (HVL), which is the thickness at which the transmission intensity is half of the initial intensity, are determined from Eq.(3) and Eq.(4):

$$\ln(N / N_0) = -\mu d \quad (3)$$

$$\mathrm{HVL} = \ln 2 / \mu \quad (4)$$

On the basis of the above results, we calculated the linear attenuation coefficient and the half value layer of 40WAlB, 50WAlB, 60WAlB and 70WAlB, and the results are shown in Table 1. Compared with concrete, the shielding performance of these materials is near and even better than that of concrete. And the HVL value of 70WAlB is just twice as much as that of pure lead.

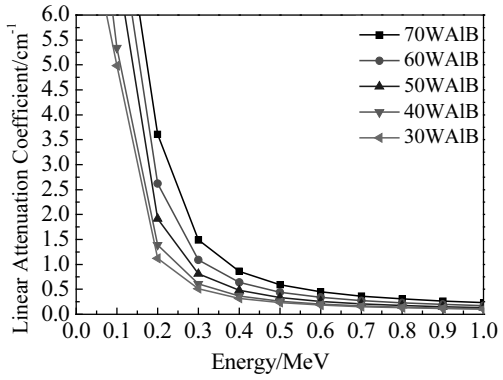

Fig.3 Relationship between the linear attenuation coefficient and energy of materials with different W contents

Table 1 Shielding properties of WAlB materials under ^{60}Co radiation

Material	μ/cm^{-1}	HVL/cm
40WAlB	0.143 24	4.84
50WAlB	0.166 18	4.17
60WAlB	0.208 38	3.32
70WAlB	0.268 29	2.58
Concrete[19]	0.20	3.51
Lead[20]	0.58	1.2

1.2 Material preparation

In this study, powders of 6061Al alloy, W (Beijing Xingrongyuan Technology, Co., Ltd, China) and B (Shanghai Aladdin Biochemical Technology, Co., Ltd, China) were used as initial materials with a purity of 99.9%. The SEM images of initial powders are shown in Fig.4. As can be seen from Fig.4c, there are cracks and voids on the W particle surface due to the large particle size. In order to obtain the average particle size of each powder, we used Nano Measurer software and calculated size of 100 particles of each powder from the SEM images. As a result, the average particle size of 6061Al, W and B powders is 13.6, 53.5, and 1.4 μm, respectively.

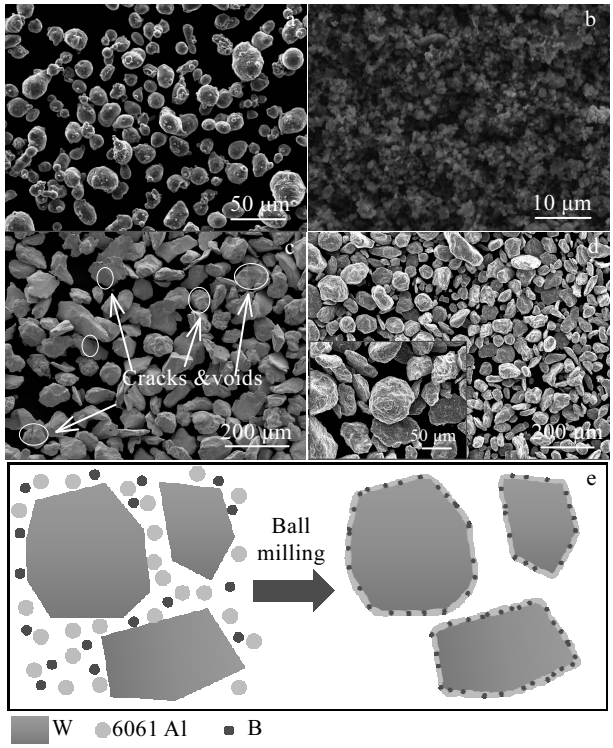

Fig.4 Morphologies of raw materials: (a) 6061Al alloy, (b) B, (c) W, and (d) mixed powders; (e) schematic sketch of mixed powders through ball-milling

Based on the simulation results, we fabricated composites with different compositions (40WAlB, 50WAlB, 60WAlB and 70WAlB) and pure 6061Al as a comparison. First, the W, B and 6061Al powders were mixed evenly by ball-milling (GN-2) under argon atmosphere at a speed of 1000 r/min for 10 h, and the mass ratio of power to ball is 5:1. Agate balls with diameters of 10, 8 and 5 mm were used as grinding media. Fig.4d shows the SEM images of the mixed powders of 50WAlB. As can be seen, the large W particles are coated with small Al and B particles, and almost no single Al and B particles are observed. This is because during the high-speed and long-time ball milling process, soft Al and B particles were prone to plastic deformation while the W particles were difficult to deform due to their high hardness. Besides, the particle size of Al and B is much smaller than that of W. Therefore, Al and B particles were easily to adhere to the surface of W particles under the action of grinding balls. The coverage of Al and B particles can effectively avoid the direct contact of W particles during sintering process. To compare the morphology of W particles before and after ball milling, it is found that the surface of W particles becomes much smoother after ball milling. And the decrease of sharp corners of W particles is beneficial to the reduction of stress concentration when preparing composite materials. The schematic sketch of ball milling process is given in Fig.4e.

Then, the mixed powders were loaded into a graphite die of 30 mm in diameter with graphite foils to segregate powder and punches. The powder samples were sintered at 570 ^{o}C for 5 min by spark plasma sintering (SPS, DR. SINTER SPS331-Lx, Japan) under a vacuum atmosphere. A uniaxial pressure of 40 MPa was applied throughout the process. After sintering, the sintered billets were heated in a furnace at 500 °C for 15 min and then rolled into composite sheets with the same total reduction (60%) at a rolling speed of 20 mm/s.

The Archimedes principle was used to measure the relative density of as-rolled (W+B)/6061Al composites and pure 6061Al alloy. The microstructure of all samples was evaluated by scanning electron microscopy (SEM, JSM-6700F) equipped with an energy-dispersive spectrometer (EDS) and an electron backscatter diffraction (EBSD). The phase analysis was performed in an X-ray diffractometer (XRD) using Cu Kα radiation. The tensile tests were conducted at room temperature and a rate of 0.5 mm/min. For each sample, three specimens were tested. Fracture surfaces after the tensile tests were examined by SEM.

2 Results and discussion

2.1 Microstructure and density of (W+B)/6061Al composites

Fig.5 shows SEM images of the composites with W content from 40 wt% to 70 wt%. As can be seen, after rolling, the distribution of W particles is relatively homogeneous in the composite except for agglomeration in samples with higher W content. The agglomeration will lead to higher W-W contiguity. In other words, the direct contact of W particles increases the W-W interface, which has poor combination because of the absence of metallurgical bonding. Besides, little plastic deformation can occur in W particles (the melting point is 3410 °C) due to the lower temperature of fabrication process. Therefore, the W particles are loosely distributed in the matrix and thus cause the decrease of mechanical properties.

Table 2 shows the values of density and relative density of the (W+B)/6061Al composites. The actual density of each sample was measured 3 times to get an average value. With the increase of W content, the density of composites decreases from 98.78% (40WAl) to 97.93% (70WAl), all lower than that of pure 6061Al alloy fabricated under the same condition. Combined with the SEM images shown in Fig.5, the decrease of density can be attributed to the increase of W agglomeration. As discussed above, the increase of W content will lead to more W-W contiguity which has poor interfacial bonding. Thus, some minor defects at W-W interfaces will result in the decrease of density.

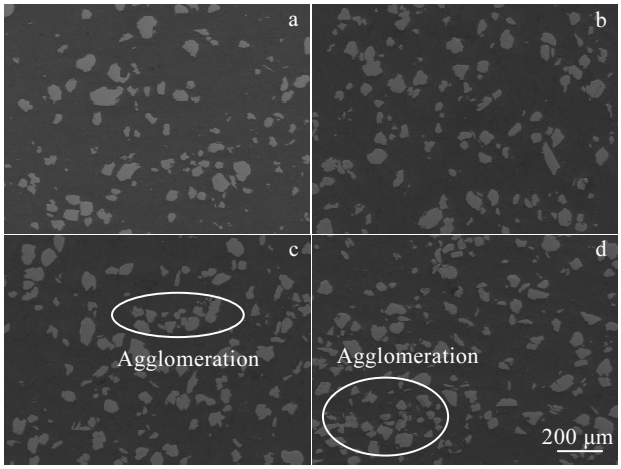

Fig.5 SEM images of (W+B)/6061Al composites with different W contents: (a) 40 wt%, (b) 50 wt%, (c) 60 wt%, and (d) 70 wt%

Table 2 Density of prepared (W+B)/6061Al composites

W content/ wt%	Measured density/g·cm^{-3}	Theoretical density/g·cm^{-3}	Relative density/%
0 (6061Al)	2.69	2.70	99.63
40	4.06	4.11	98.78
50	4.66	4.72	98.73
60	5.47	5.56	98.38
70	6.61	6.75	97.93

2.2 Interface analysis and phase identification

Fig.6 shows the SEM and EDS spectrum of W-Al interface. From the magnified image shown in Fig.6a, the interface of W-Al is relatively flat and smooth without any voids and cracks, indicating that the interface is bonded well. The EDS mapping shows that the diffusion of element Al is more severe than that of elemental W. According to Tang's work[21], the diffusion rate of Al is much higher than that of W, and the extremely high melting point of W also leads to higher diffusion activation energy compared with Al. Besides, the diffusion of W and Al elements is all restricted and there is no obvious interface reaction layer. As shown in Fig.6d, the line EDS results also reveal that there is a certain diffusion layer at the W-Al interface. From Huang's work[22], according to the Hume-Rothery rules, good solubility can exist between Al and W. From the XRD results shown in Fig.7, only W and Al diffraction peaks are clearly observed, whereas Al-W intermetallics (such as Al_5W, Al_4W and $Al_{12}W$) are not detected. Thus, from SEM/EDS and XRD results, it can be confirmed that the element solid solution mainly exists at the interface of W-Al rather than intermetallics. This can be attributed to the low fabrication temperature and large particle size. The sintering temperature (570 °C) and rolling temperature (500 °C) are far below the melting point of W, and the holding time of SPS process is only 5 min which is much shorter than the holding time of traditional sintering methods. So the energy and time of elements are insufficient to diffuse and to form intermetallics. In addition, large W particles have low specific surface area, which leads to low surface energy. Therefore, the reaction of W-Al is restricted. Besides, the absence of B peak in XRD results may be caused by its low content. And because of its small particle size, it is hard to analyze the interfacial behavior of Al-B. So in this study, we just put emphasize on W and its effect on the composite.

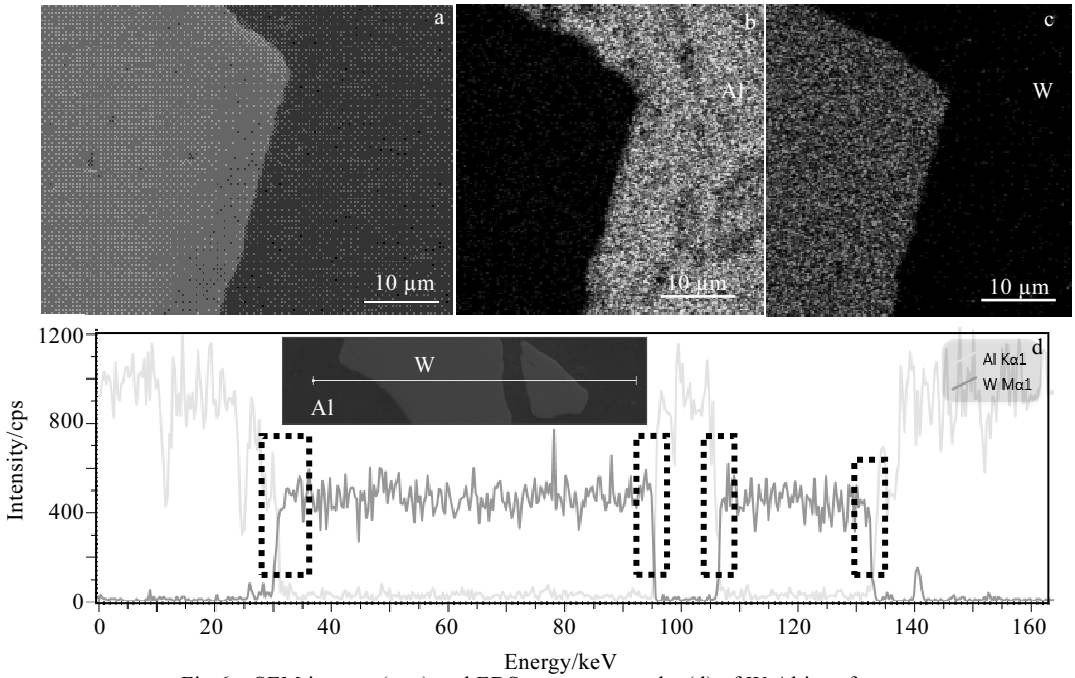

Fig.6 SEM images (a~c) and EDS spectrum results (d) of W-Al interface

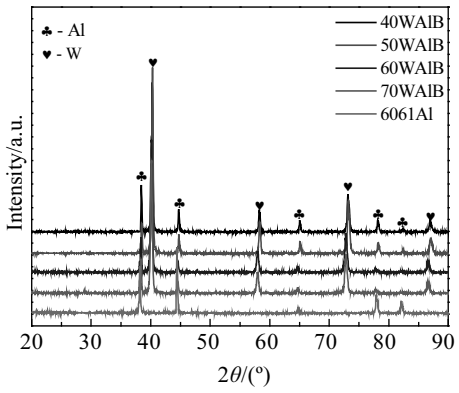

Fig.7 XRD patterns of (W+B)/6061Al composites and 6061Al

2.3 EBSD analysis

Fig.8 shows the EBSD results of as-rolled 50WAlB composite. Fig.8a is the phase map where red and blue areas represent Al and W, respectively. As can be seen, apart from the large W particles, there are also small particles in the Al matrix. Fig.8b presents the location of different grains by three grain boundary colors. High-angle grain boundaries (HAGBs) with misorientation greater than 15° are represented by black lines, low-angle grain boundaries (LAGBs) with misorientation between 2°~15° are represented by green lines, and blue lines represent twins. As shown, both HAGBs and LAGBs are distributed in the composite. Fig.8c shows the percentage of grain size

distribution (Fx(x)), and it cn be seen that 6061Al grains smaller than 5 μm occupy the majority of the composite and the average grain size is 2.43 μm. Therefore, the rolling process can significantly reduce the grain size of 6061Al matrix. Besides, in the areas around W particles (especially the small dispersed ones), grains are much smaller than those in the areas away from W particles. This is because of the higher recrystallization nucleus rate in the areas around W particles[23]. As shown in Fig.9, dynamic recrystallization (DRX) takes place during the rolling process. The DRX grains mainly exist in the areas around W particles and the grain size in these areas is much smaller. During deformation process, the degree of plastic deformation of W particles and 6061Al matrix is quite different. This incongruent plastic deformation results in different strains of 6061Al matrix around W particles and causes an area with enforced strain gradient. The enforced strain gradient can create a region with high density of dislocation and large orientation gradient, which is also known as particle deformation zone (PDZ). And this area is favorable for the development of recrystallization nucleus[24]. Therefore, the grain size of Al is much smaller in the region near W particles. Fig.10 shows the local strain distribution of the composite. As can be seen, the strain is uniformly distributed at the grain boundaries and the maximum strain distribution is located in the areas with fine grains around W particles. This is also caused by the deformation incompatibility between the non-deformed W particles and the Al matrix.

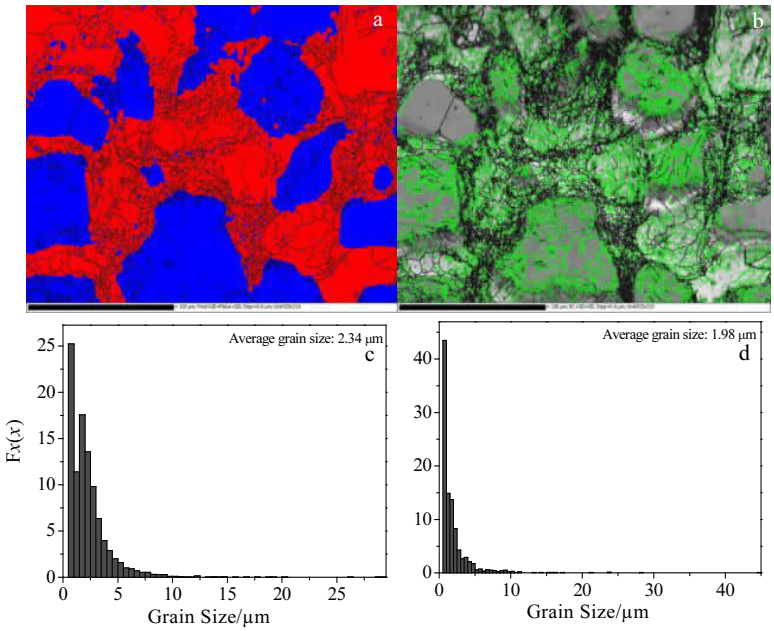

Fig.8 EBSD results of as-rolled 50WAlB composite: (a) phase map; (b) microstructure; (c, d) grain size distribution

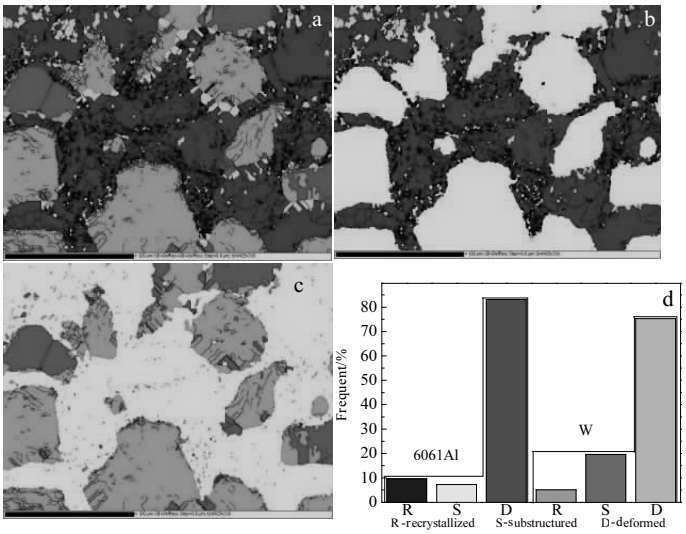

Fig.9 EBSD maps showing recrystallized, substructured and deformed region of composite: (a) total map; (b, c) layered maps; (d) color indicator image

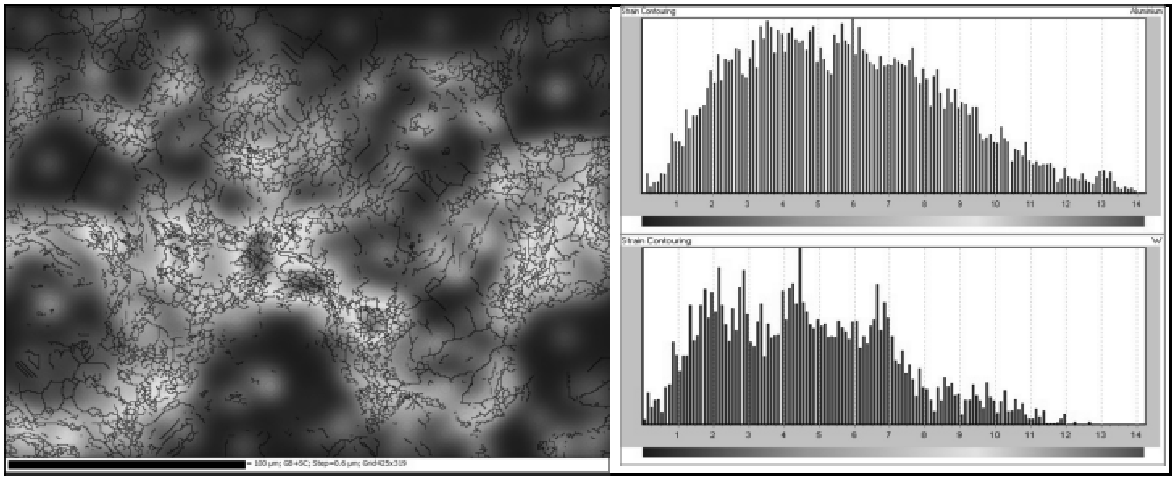

Fig.10 Local strain distribution of composite

The orientation distribution of Al is shown in Fig.11a. The orientation of Al is random in the (001), (101), and (111) crystal planes. As shown, there is no significant difference in the proportion of grains with different orientations. From Fig.11c, the multiple uniform density (MUD) of the composite is only 4.1, which indicates that there is no obvious texture in the composite. In order to further confirm the orientation distribution of Al matrix grains, the misorientation distribution of the matrix Al was carried out in this region, as shown in Fig.11b. The "correlated" curve means misorientation calculated from neighboring points, "uncorrelated" means misorientation calculated from random points in scanning, and "random" represents the misorientation distribution between grains under the condition of random orientation without texture. The peak value of random misorientation in a typical cubic system is at 45°. It can be observed that the distribution of misorientation (blue) at random points is basically consistent with the theoretical distribution of misorientation (green). This indicates that after rolling, there is no texture in the matrix Al grain of composites, which also shows that the existence of W particles can weaken the texture of grain significantly. Hence, the fabricated composite has near isotropic property, which can lead to favorable mechanical properties.

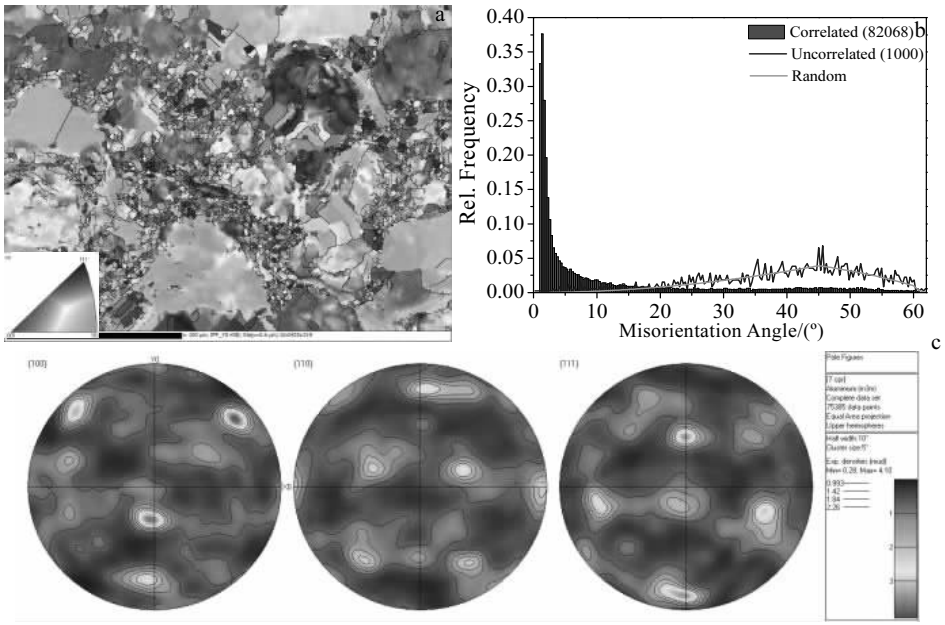

Fig.11 Orientation distribution of Al (a); misorientation angle distribution of matrix Al (b); and multiple uniform density (MUD) of the composite (c)

2.4 Tensile properties of (W+B)/6061Al composites

Fig.12 shows the ultimate tensile strength (UTS) and elongation to fracture of 6061Al alloy and (W+B)/6061Al composites. As can be seen, the tensile strength of the composites increases first and then decreases with the increase of W content, all higher than that of pure 6061Al alloy fabricated under the same condition, while the elongation to fracture is almost decreased compared to that of 6061Al alloy. The higher strength of all composites is mainly attributed to dislocation strengthening and load transfer effect. In this case, the large difference in the coefficient of thermal expansion between Al matrix (23.86×10^{-6} K^{-1}) and W particles (4.5×10^{-6} K^{-1}) leads to higher dislocation density around the W particles. Besides, the load transfer effect introduced by W particles plays the main role. As shown in Fig.6, the interface between W particles and the matrix achieves a good bonding without obvious intermetallics but an element solid solution. The favorable interfacial bonding can effectively transfer the loads from matrix to W particles, thus improving the strength of composite. Due to the large particle size of W (50 μm), Orowan strengthening is not suitable in this case. Among all composites, 50WAlB shows the highest strength of 240.2 MPa. And the lower strength of 60WAlB and 70WAlB can be explained as follows: the W particles with a large size used in this study contain more defects, which makes the load capacity decrease. Besides, the aggregation of W becomes more sever in these composites, which also has unfavorable effects. So with higher W content, the composites show much poor mechanical properties.

Fig.13 shows the tensile fracture surfaces of pure 6061Al alloy and (W+B)/6061Al composites. As shown, the fracture surfaces of (W+B)/6061Al composites with different W contents show similar characteristics, including both ductile and brittle fractures. With the increase of W content, the fracture surface shows particle aggregation, which is the reason for declining in mechanical properties. From Fig.13f, the clear contour exists at the fracture surface due to the pull-out of particles. In addition, there are obvious pits on the surface of exposed W particles, which may be the defects inside the particles. These defects are voids which exist in the original particles, as shown in Fig.4c. These defects can be sources of potential cracks during tensile test, and the cracks propagate from the crack source and lead to the fracture of W particles, producing clean W particle surfaces. Fig.13g shows the interfacial debonding between W particle and Al alloy matrix. As can be seen, a large crack forms between the particle and the matrix. This is because under the action of shear force, the degree of plastic deformation of W particles is quite different from that of base Al alloy. The plastic deformation of the matrix is large while W particles hardly deform. This uncoordinated deformation results in greater stress concentration at the sharp corner of W particles, and when the stress is higher than the bonding strength at the interface, the crack will preferentially occur at the sharp corner of W particles. In Fig.13h, tearing ridges of matrix Al alloy exist on the edge of exposed W particles. Compared with the particle in Fig.13g, the surface of W particle is much

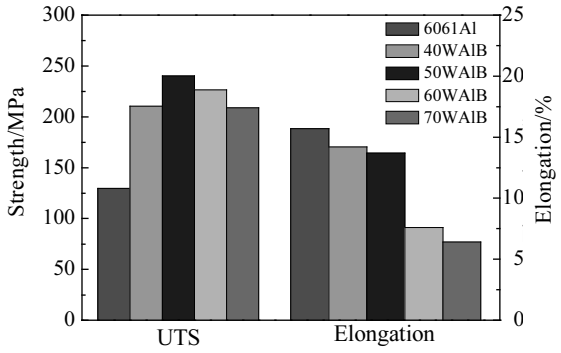

Fig.12 Ultimate tensile strength (UTS) and elongation to fracture of 6061Al alloy and (W+B)/6061Al composites

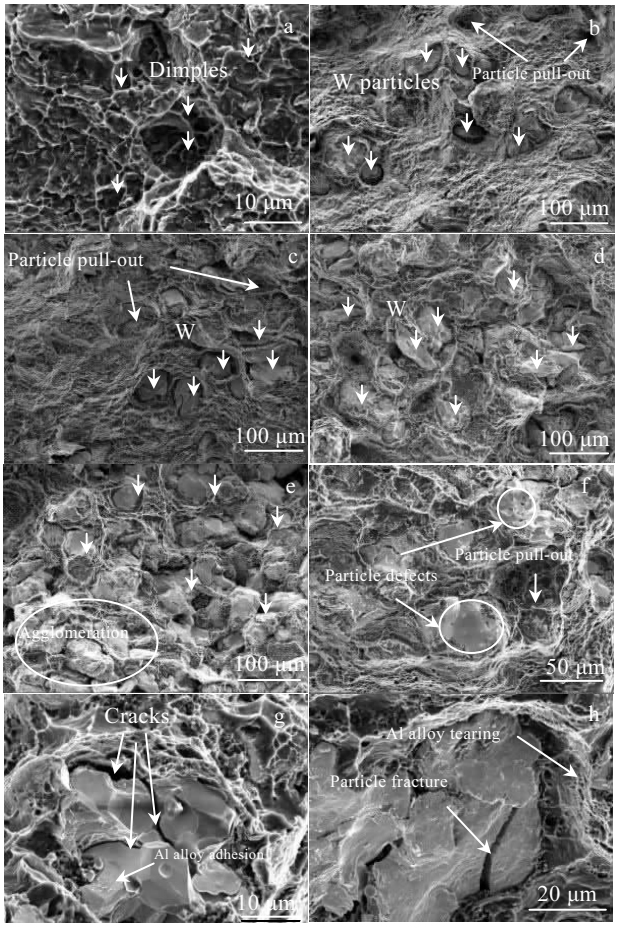

Fig.13 Tensile fracture surfaces of pure 6061Al alloy (a) and (W+B)/6061Al composites with different W contents: (b) 40 wt%, (c) 50 wt%, (d) 60 wt% and (e~h) 70 wt%

rougher, which is caused by the tearing between W particle and the matrix Al alloy during tensile process. Besides, the particle fracture is obvious on the fracture surfaces. Because the particle size of W is relatively large in this case, the interface area between each single W particle and the matrix is larger. Thus, each single W particle needs to bear more load transferred from matrix during the tensile process. The large particle size also brings more defects, which makes W particles easier to fracture. Therefore, the failure mode of the composites includes the interfacial debonding and the cleavage fracture of particles. Fig.14 shows the schematic sketch of crack initiation in (W+B)/6061Al composite during tensile test.

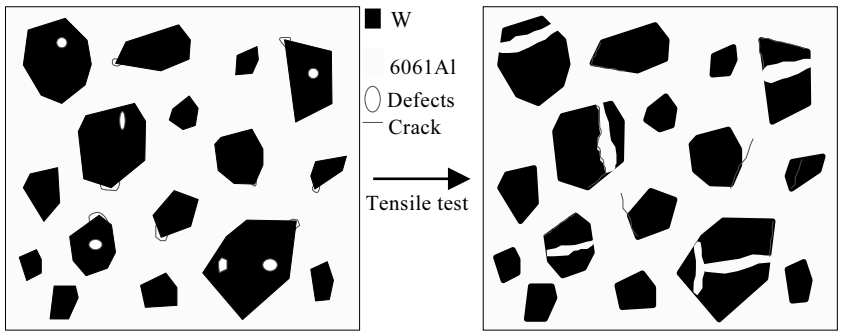

Fig.14 Schematic sketch of crack initiation in the (W+B)/6061Al composite during tensile test

3 Conclusions

1) The neutron transmission ratio decreases with the increase of W particle content and the thickness of the composites plates. The relationship between the neutron transmission ratio and thickness of the composites with different W contents is determined as follows: y(30 wt%)=$e^{-1.74174x}$, y(40 wt%)=$e^{-1.89881x}$, y(50 wt%)=$e^{-2.17795x}$, y(60 wt%)=$e^{-2.56168x}$, y(70 wt%)=$e^{-3.10464x}$.

2) The linear attenuation coefficient of the composites against gamma ray increases with the increase of W content. The linear attenuation coefficient of 40WAlB, 50WAlB, 60WAlB and 70WAlB against ^{60}Co (1.25 MeV) is 0.143 24, 0.166 18, 0.208 38 and 0.268 29 cm^{-1}, respectively.

3) Tungsten and boron particles are homogeneously distributed along the aluminum alloy matrix after ball-milling, SPS and hot-rolling processes. EDS and XRD results show that no pronounced interfacial reaction occurs at the interface of tungsten and 6061Al alloy, where solid solution mainly exists. The phases of the composites are mainly W and Al.

4) The W particles can promote the dynamic recrystallization nucleation, restrain the grain growth and reduce the texture of aluminum matrix.

5) The mechanical tests show that with the increase of W particle content, the strength of (W+B)/6061Al composites increases first and then decreases while elongation to fracture is almost decreased. The failure mode of the composites is mainly interfacial debonding and cleavage fracture of particles.

6) Among all the fabricated composites, 50WAlB shows relatively good radiation shielding properties, the highest tensile strength and good plasticity. The material with this composition is worthy of further experimental study.

References

1 Chen Feida, Ni Minxuan, Tang Xiaobin *et al*. *Journal of Physics and Chemistry of Solids*[J], 2018, 119: 258
2 Vishwanath P Singh, Badiger N M. *Annals of Nuclear Energy*[J], 2014, 64: 301
3 Sercombe T B. *Materials Science and Engineering A*[J], 2003, 363: 242
4 BasturkM, Arztmann J, Jerlich W *et al*. *Journal of Nuclear Materials*[J], 2005, 341: 189
5 Shina Ji Wook, Leea Jang-Woo, Yu Seunggun *et al. Thermochimica Acta*[J], 2014, 585: 5
6 Chen H S, Wang W X, Li Y L *et al. Journal of Alloys and Compounds*[J], 2015, 632: 23
7 Yoshinori Sakurai, Akira Sasaki, Tooru Kobayashi. *Nuclear Instruments and Methods in Physics Research Section A*[J], 2004, 522: 455
8 Zhang Peng, Li Yuli, Wang Wenxian *et al. Journal of Nuclear Materials*[J], 2013, 437: 350
9 Giménez M A N, Lopasso E M. *Annals of Nuclear Energy*[J], 2018, 116: 210
10 Chen H S, Wang W X, Li Y L *et al. Materials & Design*[J], 2016, 94: 360
11 Susanta K Pradhan, Subhranshu Chatterjee, Amitava Basu Mallick *et al. Perspectives in Science*[J], 2016, 8: 529
12 Gaurav Bajpai1, Rajesh Purohit1, Ranal R S *et al. Materials Today Proceedings*[J], 2017, 4: 2723
13 Dhanashekara M, Senthil Kumarb V S. *Procedia Engineering*[J], 2014, 97: 412
14 Nassar Amal E, Nassar Eman E. *Journal of King Saud University-Engineering Sciences*[J], 2017, 29: 295
15 Eldesouky A, Johnsson M, Svengren H *et al. Journal of Alloys*

and Compounds[J], 2014, 609: 215
16 Dash K, Chaira D, Ray B C. *Materials Research Bulletin*[J], 2013, 48: 2535
17 Orru R, Licheri R, Locci A M *et al. Materials Science and Engineering R*[J], 2009, 63: 127
18 El-Sayed A Walya, Michael A Fusco, Mohamed A Bourham *et al. Annals of Nuclear Energy*[J], 2016, 96: 26
19 Gerward L, Guilbert N, Jensen K B *et al*. *Radiation Physics and Chemistry*[J], 2004, 71: 653
20 Ahmed S Ouda. *HBRC Journal*[J], 2015, 79: 48
21 Tang H G, M X F, Zhao W *et al. Journal of Alloys and Compounds*[J], 2002, 347: 228
22 Huang Guoqiang, Shen Yifu, Guo Rui *et al. Materials Science and Engineering A*[J], 2016, 674: 504
23 Chen H S, Wang W X, Nie H H *et al. Vacuum*[J], 2017, 143: 363
24 Doherty R D, Hughes D A, Humphreys F J *et al. Materials Science and Engineering A*[J], 1997, 238: 219

一种由 MCNP 设计，通过 SPS 加热轧制的新型辐射屏蔽复合材料

张宇阳[1]，王文先[1]，陈洪胜[1,2]，刘瑞峰[1]，张媛琦[1]，石 宁[1]
(1. 太原理工大学 山西省先进镁基材料重点实验室，山西 太原 030024)
(2. 太原理工大学 机械与运载工程学院，山西 太原 030024)

摘 要：设计和制备了一种新型的中子和 γ 射线辐射屏蔽复合材料。基于蒙特卡罗模拟，首次采用球磨法和 SPS 加热轧制法制备了不同 W 含量(40%~70%，质量分数)的新型(W+B)/6061Al 复合材料，并对其组织和力学性能进行了研究。实验结果显示，轧制之后，W 和 B 颗粒均匀分布于基体中，而且 W/Al 界面以固溶体的形式呈现出良好的冶金结合。复合材料的物相主要包括 W 和 Al。EBSD 结果表明，W 颗粒具有促进动态再结晶(DRX)成核、限制晶粒长大和降低 6061Al 基体织构的作用。拉伸试验表明，W 含量为 50%的复合材料强度最高，塑性较好。结合模拟结果，该组分的复合材料性能达到了实际应用要求。(W+B)/6061Al 复合材料的强化机理包括位错强化和载荷传递效应。

关键词：(W+B)/6061Al；辐射屏蔽复合材料；显微组织；力学性能；强化机理

作者简介：张宇阳，男，1992 年生，硕士生，太原理工大学材料科学与工程学院，山西 太原 030024，E-mail: 245509439@qq.com